

Real-space Imaging of Spin Stripe Domain Fluctuations in a Complex Oxide

Longlong Wu^{1,2*}, Yao Shen¹, Andi M. Barbour³, Wei Wang¹, Dharmalingam Prabhakaran⁴, Andrew T. Boothroyd⁴, Claudio Mazzoli³, John M. Tranquada¹, Mark P. M. Dean¹ and Ian K. Robinson^{1,5†}

¹*Condensed Matter Physics and Materials Science Department, Brookhaven National Laboratory, Upton, NY 11973, USA*

²*Computational Science Initiative, Brookhaven National Laboratory, Upton, NY 11973, USA*

³*National Synchrotron Light Source II, Brookhaven National Laboratory, Upton, New York 11973, USA*

⁴*Department of Physics, University of Oxford, Clarendon Laboratory, Oxford OX1 3PU, United Kingdom*

⁵*London Centre for Nanotechnology, University College London, London, WC1E 6BT, United Kingdom.*

Supplementary Figures:

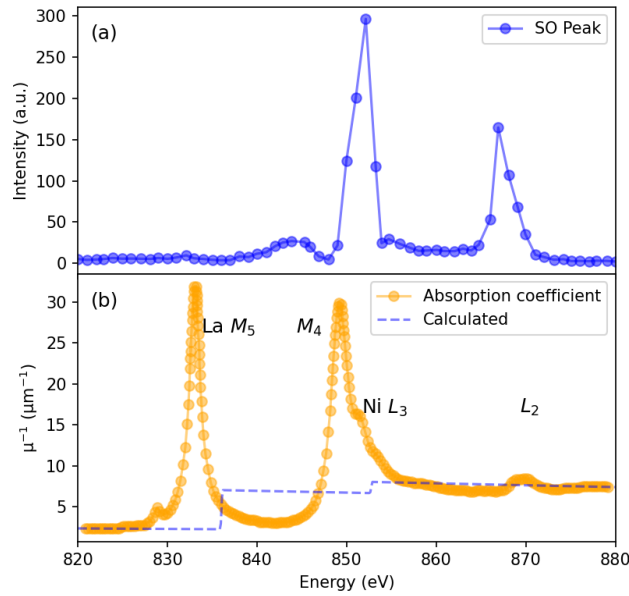


FIG. S1 (a) Experimental intensities of the (0.36, 0.36, 0) spin-order superstructure peak as a function of photon energy at 70K for π -polarized x-rays. π -polarized x-rays were used to enhance the magnetic signal from the sample and reduce background. (b) Estimated x-ray absorption coefficient for the LSNO sample. This was completed by scaling the pre-edge and post-edge regions of the x-ray absorption coefficient with the calculated one as labeled by blue dashed line in (b) [1]. The corresponding x-ray absorption spectrum is extracted from Ref. [2] for a similar sample to ours. We can estimate from (b) that the estimated penetration depth is ~ 69 nm when the energy of the incident x-ray is 852 eV and the incidence angle α_i of the x-ray is 75.4° .

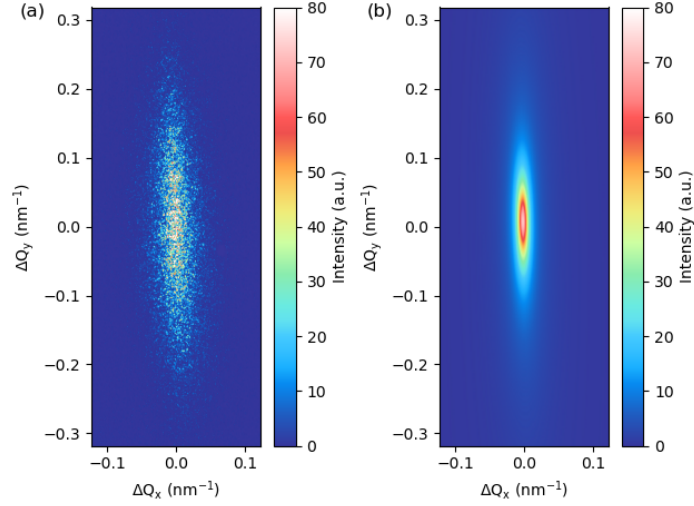


FIG. S2 (a) Representative coherent x-ray diffraction patterns from the SO superlattice peaks at $\mathbf{Q} = (0.36, 0.36, 0)$, which is measured with an $8\ \mu\text{m}$ pinhole. Here, $\Delta\mathbf{Q} = \mathbf{q} - \mathbf{Q}$ and \mathbf{q} is the scattering wavevector transfer. (b) Result of a 2D fit of (a) to a Lorentzian squared function.

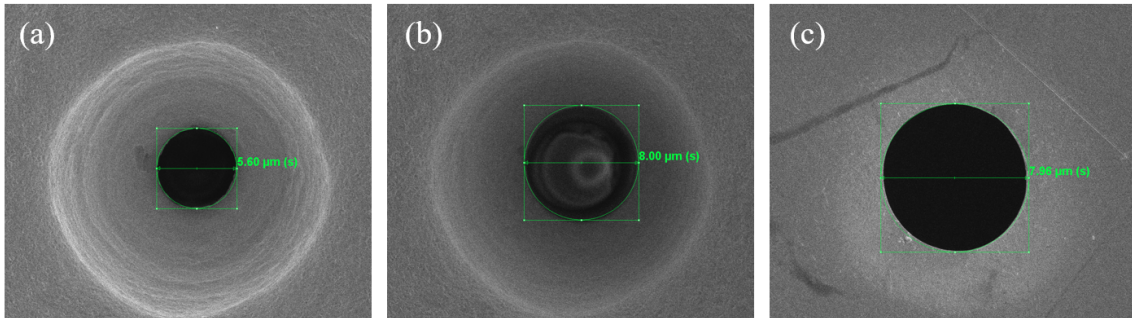


FIG. S3 Scanning electron microscope images of the pinhole before and after Focused Ion Beam (FIB) polish. (a) Back view of the pinhole before FIB polish. (b) Back view of the pinhole after FIB polishing. (c) Front view of the pinhole after FIB polishing.

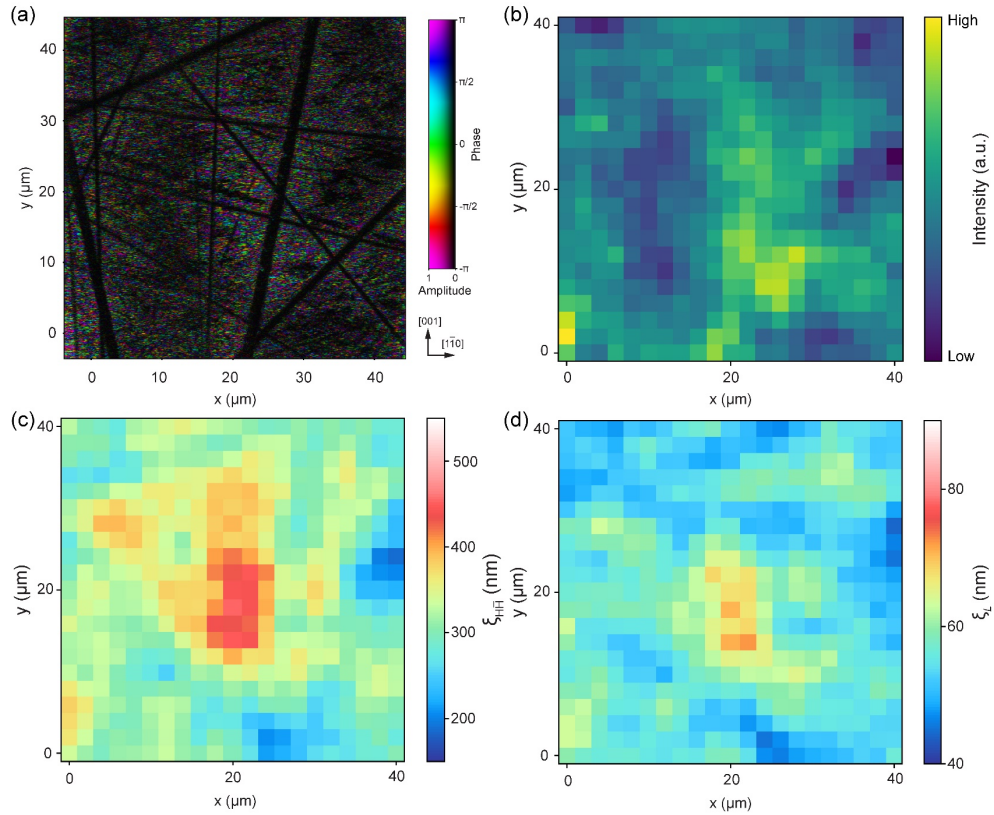


FIG. S4 (a) Representative ptychographic image of SO stripe domains over a large scale. The image has been aligned to the crystal orientation of the LSNO sample as shown in the legend of the figure. Here, the amplitude is represented by the brightness of the image and the phase is rendered by the hue. (b) Integrated coherent x-ray diffraction intensity. (c) SO domain size along $[1\bar{1}0]$. (d) SO domain size along $[001]$ directions. The most striking features in (a) are the straight dark lines which resemble the scratches due to crystal polishing. It is possible the scratches are filled by $(1\bar{1}0)$ SO stripe domains, but we suspect the disappearance of the SO domains in these regions may result from the surface damage of the sample due to polishing.

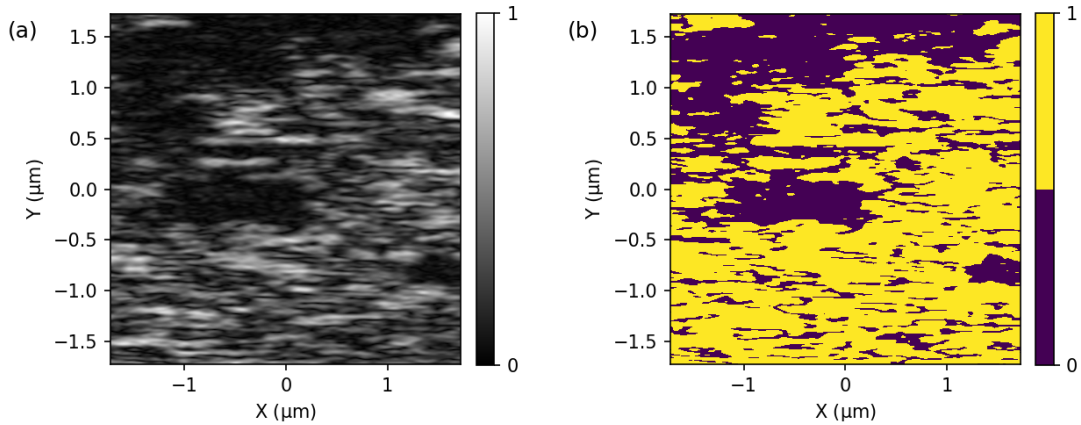


FIG. S5 (a) Amplitude distribution of the ptychographic SO stripes image in Fig. 3(a). (b) Binarization of the amplitude of the SO stripes image in (a). The filling fraction of the SO along [110] direction in the above image is 0.62. This is estimated by using the amplitude of the SO stripes in the image with a threshold for the binarization of 15% of the maximum amplitude of the SO images. Even taking into account these large dark regions which are suspected to be the surface damage, the ratio is still greater than 0.5. This suggests the SO has a preferred (110) domain orientation near the surface.

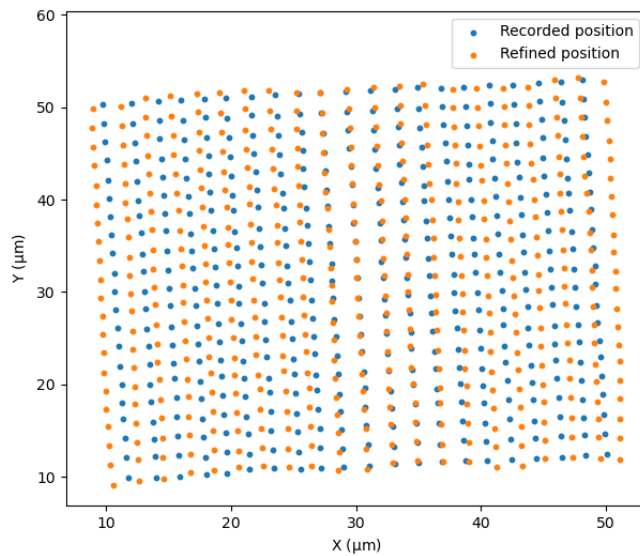


FIG. S6 Plot of the refined positions for the reconstruction of LSNO data. Here, the blue dots represent the recorded x-ray probe positions in the detector frame on the LSNO sample during the ptychography experiment. The orange dots show the refined x-ray probe position in detector frame by using the annealing method.

Supplemental Methods:

LSNO Crystal Growth:

A polycrystalline sample of composition $\text{La}_{1.775}\text{Sr}_{0.225}\text{NiO}_{4-d}$ was prepared using high purity (>99.99%) starting materials La_2O_3 (preheated at 1100 °C for 12h before weighing), SrCO_3 and NiO (preheated at 350 °C for 12h) by the solid-state reaction technique at 1200-1300 °C for 72h with intermittent grinding. Feed rods of 10mm diameter and 100 mm length were prepared using the single-phase polycrystalline powder and the rods were sintered at 1450 °C for 12h. Crystal growth was carried out using a four-mirror optical floating-zone furnace (Crystal Systems Inc.). During crystal growth, argon and oxygen mixed gas of ratio 9:1 with a pressure of 5.5 bar was maintained. Crystals were grown at a rate of 4 mm/h with the seed crystal and feed rod counter rotating at 30 rpm.

Soft X-ray Experiments:

Resonant soft X-ray Ptychography measurements were carried out at the Coherent Soft X-ray Scattering (CSX) beamline, National Synchrotron Light Source II, Brookhaven National Laboratory. The energy of the incident x-ray was tuned at 852 eV, corresponding to the Ni L_3 -edge of the LSNO sample, which gave the strongest signal. The X-ray beam was collimated by an 8 μm pinhole in diameter located ~ 5.5 mm before the sample. The LSNO sample was mounted on a three-circle in-vacuum diffractometer in a helium-flow cryostat. The coherent x-ray diffraction signal was recorded by an in-vacuum CCD area detector (Berkeley Fast CCD, 960 \times 960 pixels, 30 \times 30 μm^2 pixel size) located 0.34 m away from the sample. The LSNO sample was cooled down to 70K by the cryostat. When doing the ptychography raster scan, the step size was 2 μm in a simple mesh. The exposure time for each coherent x-ray diffraction pattern was 2s.

FIB Prepared Pinhole:

An unpolished ~ 5 μm pinhole, laser drilled into a $\text{Pt}_{95}\text{Ir}_5$ foil, was purchased from Ted Pella, Inc then milled to 8 μm diameter by utilizing focused-ion beam milling in a FEI Helios 600 dual-beam scanning electron/focused ion beam microscope. The “circle” pattern was chosen for the milling. In order to get a smooth border in the pinhole, a 30 keV Ga ion beam with 93 pA beam current was applied to polish the inside of the pinhole from both sides.

X-ray Absorption Coefficient:

Here, the absorption coefficient μ is estimated by [3]:

$$\mu^{-1} = \frac{1}{\text{Im}(2n \cdot k)} \sin \left\{ \text{Re} \left[\text{acos} \left(\frac{\cos \alpha_i}{n} \right) \right] \right\}, \quad (\text{S1})$$

where $n(\lambda) = 1 - \delta(\lambda) + i\beta(\lambda)$ is the refractive index [4] of the LSNO sample. α_i is the incident angle of soft x-ray beam and $k = \frac{2\pi}{\lambda}$ is the wave number of the x-ray and λ is the corresponding wavelength.

Bragg Ptychographic Reconstruction:

Before the Bragg ptychographic reconstruction, the raw coherent x-ray diffraction data were processed including the measured flat field, dark field, as well as fluorescence background correction. Firstly, a dark image, which is an average of a series of 2s dark exposure, was subtracted to correct for the dark background. Then, the flat-field correction was applied for the processed data. The acquired flat field was obtained before the Bragg ptychographic measurements. In order to ensure that shot noise in the background was suppressed, an additional threshold of approximately 1 phonon (25 analog to digital units (ADUs)) was used, below which signal was zeroed after background and flat field corrections. Then, the obtained diffraction patterns were padded by zeros to a size of twice the maximum size of the extracted diffraction patterns, and this data array size was used in the iterative ptychography algorithm.

The phase retrieval of the Bragg Ptychography data set was performed on a computer with 256 GB of RAM and two NVIDIA Quadro V100 GPUs. To preserve the coherent x-ray diffraction signal information, the reconstruction was directly performed in the detector coordinates [5]. After reconstruction, the final 2D ptychography results were transformed into the laboratory frame.

For the phase retrieval algorithm, our procedure firstly used the regularized ptychographic iterative engine (PIE) [6]. Then, the Error Reduction (ER) [7] and Difference Map (DM) [8] algorithms were alternately applied during the reconstruction. Since drift and uncertainties in the probe positions are known to occur in ptychography measurements, probe position correction was also performed to remove these artifacts during the reconstruction. Here, an annealing method [9] was used for the probe position correction (Fig. S6 shows one example of the refined positions.). A total of 15000 iterations was performed for all of reconstructions. The detailed reconstructions

followed the following algorithm sequence: for the first 1500 iterations, the reconstructions were performed without the position correction. After that, the position of the probe was updated based on the annealing method for 50 iterations. The probe position correction was not applied for the last 150 iterations. During the reconstruction, the ER and DM were switched every 50 iterations.

Two-time Cross Correlation Coefficient:

For quantification of the time scale of the SO domain fluctuations, we calculated the two-time cross correlation coefficient between these obtained real space images,

$$\text{cor}(t_1, t_2) = \frac{\sum_i [S_i(t_1) - \overline{S}(t_1)] \cdot [S_i(t_2) - \overline{S}(t_2)]}{\sqrt{\sum_i [S_i(t_1) - \overline{S}(t_1)]^2 \cdot \sum_i [S_i(t_2) - \overline{S}(t_2)]^2}}, \quad (\text{S2})$$

where S_i represents the i th value of the amplitude S of the reconstructed SO image, t_1 and t_2 are the measurement time. The summations use the amplitude information from the full area of the reconstructed SO images in Fig. 3. Fig. 4(c) shows the calculated correlation coefficient as a heat map for all pairs.

Supplementary References

- [1] M. P. Dean, G. Dellea, R. S. Springell, F. Yakhou-Harris, K. Kummer, N. B. Brookes, X. Liu, Y. J. Sun, J. Strle, T. Schmitt, L. Braicovich, G. Ghiringhelli, I. Bozovic, and J. P. Hill, *Nat. Mater.* **12**, 1019 (2013).
- [2] C. Schussler-Langeheine, J. Schlappa, A. Tanaka, Z. Hu, C. F. Chang, E. Schierle, M. Benomar, H. Ott, E. Weschke, G. Kaindl, O. Friedt, G. A. Sawatzky, H. J. Lin, C. T. Chen, M. Braden, and L. H. Tjeng, *Phys. Rev. Lett.* **95**, 156402, (2005).
- [3] J. Daillant and A. Gibaud, *X-ray and Neutron Reflectivity* (Springer, Berlin Heidelberg, 2009), Lecture Notes in Physics.
- [4] B. L. Henke, E. M. Gullikson, and J. C. Davis, *At. Data Nucl. Data Tables* **54**, 181 (1993).
- [5] N. Burdet, X. Shi, J. N. Clark, X. Huang, R. Harder, and I. Robinson, *Phys. Rev. B* **96**, 014109 (2017).
- [6] A. Maiden, D. Johnson, and P. Li, *Optica* **4**, 736 (2017).
- [7] R. W. Gerchberg, *Optik* **35**, 237 (1972).
- [8] P. Thibault, M. Dierolf, A. Menzel, O. Bunk, C. David, and F. Pfeiffer, *Science* **321**, 379 (2008).
- [9] A. M. Maiden, M. J. Humphry, M. C. Sarahan, B. Kraus, and J. M. Rodenburg, *Ultramicroscopy* **120**, 64 (2012).